

# Multi-sample Couette viscometer for polymer formulations\*

Howard J Walls<sup>1,3</sup>, Robert F Berg<sup>2</sup> and Eric J Amis<sup>1</sup>

<sup>1</sup> Polymers Division, National Institute of Standards and Technology, Gaithersburg, MD 20899-8542, USA

<sup>2</sup> Process Measurements Division, National Institute of Standards and Technology, Gaithersburg, MD 20899-8364, USA

E-mail: [hjwalls@rti.org](mailto:hjwalls@rti.org)

Received 15 April 2004, in final form 19 October 2004

Published 16 December 2004

Online at [stacks.iop.org/MST/16/137](http://stacks.iop.org/MST/16/137)

## Abstract

We describe a prototype scalable viscometer aimed at facilitating rapid measurements of multiple samples. The device simultaneously measures the viscosity of four samples in an array of Couette cells. Each cell contains a rotor with an embedded permanent magnet that is driven by an oscillating magnetic field generated by a two-axis Helmholtz coil. The angular displacement of the rotors is recorded by a charge-coupled device camera. Image analysis determines the amplitude and phase of the rotors with respect to the coil's sinusoidal current. The viscosity of each sample influences the amplitude and phase of the rotor, which can be predicted with a viscously damped oscillator model. We present data for Newtonian fluids with viscosities from 50 to 2000 mPa s.

**Keywords:** combinatorial methods, combinatorial viscometer, Couette cell, high throughput materials testing, magnetic rheometer, rheology

(Some figures in this article are in colour only in the electronic version)

## 1. Introduction

Many commodity products contain polymer solutions in their formulation, whose flow properties are important to both the manufacturer and the consumer. However, predicting the flow properties of these complex, multi-component systems is a difficult art that typically relies on the cumulative experience of a senior researcher. Developing a new formulation requires the preparation and rheological testing of libraries of samples. This paper describes a viscometer that could reduce that tedious and time-consuming step.

Combinatorial and high throughput synthesis and screening for polymer materials is coming of age [1–4]. However, rheological measurements have been slow to follow. Two exceptions, arrays of piezoelectric resonators [5, 6] and particle tracking microrheology [7], use measurement

conditions with some limitations. Piezoelectric resonators operate at tens of kHz, much greater than the usual range of interest for polymeric materials  $10^{-2}$  to  $10^2$  Hz [8, 9]. Particle tracking microrheology requires introduction of tracer particles to the sample and is limited to very small strains of optically transparent samples.

The mainstay of industrial rheology has been bulk rheology in shear rheometers or pressure-driven capillary viscometers. We are, therefore, developing a new combinatorial rheometer that is scalable and adaptable to a variety of problems in the polymer formulations industry. In its present form we measure only linear viscosities and thus refer to the instrument as a viscometer. However, the operating principles could be extended to include complex viscosity given the very nature of the measurement, dynamic oscillation.

At the heart of our multi-sample viscometer is a magnetic field that simultaneously drives all of the test cells and a single video detector that measures their responses. Previous researchers have used magnetic fields to drive a viscometer or rheometer with shapes varying from oscillating or suspended spheres and needles [10–15] to rotating discs and cylinders

\* This is an official contribution of the National Institute of Standards and Technology; not subject to copyright in the United States.

<sup>3</sup> Present address: Research Triangle Institute International, Research Triangle Park, NC 27709-2194, USA.

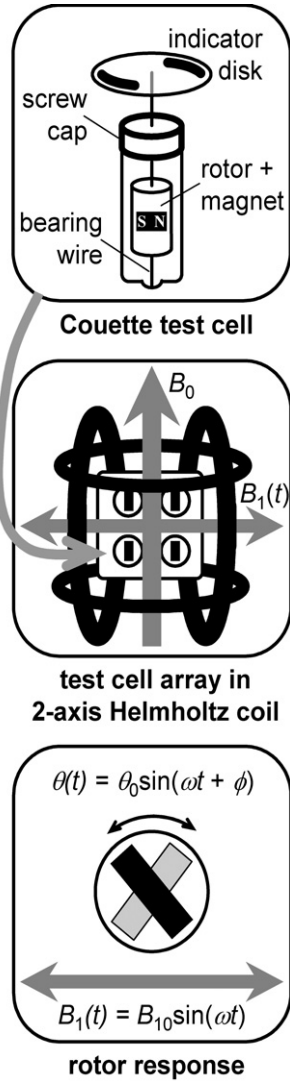


**Figure 1.** Multi-sample viscometer concept.

[16, 17]. However, as far as we are aware, we are the first to use magnetic fields to simultaneously drive multiple test cells, each containing a different sample.

In this paper, we describe the concept and working theory for the viscometer, present details of the apparatus and show preliminary results for Newtonian fluids. The initial success in modelling data for Newtonian fluids suggests that our approach can be extended to a multi-sample rheometer for complex (i.e., linear viscoelastic) fluids.

## 2. General description and model of the instrument

Figure 1 illustrates the basic idea of the instrument. Each test cell contains a rotor with a small embedded permanent magnet. An array of the test cells is placed in a two-axis Helmholtz coil. A static magnetic field  $B_0$  aligns the array of rotors while a sinusoidal magnetic field  $B_1(t)$ , orthogonal to  $B_0$ , perturbs the rotors. The sample's material properties (viscosity and density) in each test cell determine the amplitude  $\theta_0$  and phase  $\phi$  response of the rotor.

During a measurement,  $B_0$  is held constant and the amplitude  $B_{10}$  and frequency  $f$  of  $B_1(t)$  are controlled. A charge-coupled device (CCD) camera records the angular displacement of an indicator disc attached to the upper rotor bearing wire. Image analysis software determines the amplitude of the rotor's angular displacement and the phase difference  $\phi$  relative to  $B_1(t)$ .

The relation between the applied torque  $N(t)$  and the angular displacement  $\theta(t)$ , when friction and second-order effects are ignored, is

$$N(t) = k\theta + v\dot{\theta} + I\ddot{\theta}. \quad (1)$$

(See appendix A.) Here,  $v$  is the viscous dissipation coefficient and  $I$  is the rotor's moment of inertia. The torsion spring constant  $k$  is determined primarily by the product of  $B_0$  and the magnetic moment of the embedded magnet. The viscous dissipation coefficient can be approximated by that of an oscillating plane separated by a distance  $L$  from a parallel stationary plane. Equating the plane area with the area of the rotor's cylindrical surface leads to

$$v \approx \frac{2\pi(1+i)R^3H\eta}{\delta \tan[(1+i)L/\delta]}. \quad (2a)$$

(See appendix B.) Here,

$$\delta \equiv \left[ \frac{2\eta}{\rho\omega} \right]^{1/2} \quad (2b)$$

is the viscous penetration length [18], where  $\eta$  is the dynamic viscosity,  $\rho$  is the fluid density and  $\omega = 2\pi f$  is the angular frequency. In equation (2),  $H$  and  $R$  are the rotor height and radius and  $L$  is the gap between the rotor and cell's inner diameter. The rotor's moment of inertia is approximately

$$I \approx (\pi/2)\rho_r R^4 H, \quad (3)$$

where  $\rho_r$  is the density of the rotor. The range of measurable viscosities may be tuned by adjusting  $B_0$ ,  $B_{10}$  and  $L$ .

Equations (1)–(3) describe the device well when viscous damping is large compared to friction at the bearings. To solve equation (1) for the angular amplitude, we will represent the torque and angular response by their complex Fourier counterparts,

$$N(t) = N_0 e^{i\omega t}, \quad (4a)$$

$$\theta(t) = \theta_0 e^{i\omega t} e^{i\phi}. \quad (4b)$$

Dividing the Fourier transform of equation (1) by  $k\theta_0 e^{i\phi}$  yields

$$\frac{N_0}{k\theta_0 e^{i\phi}} = 1 + i \frac{v\omega}{k} - \frac{I\omega^2}{k}. \quad (5)$$

Making use of equations (2) and (3), and recognizing  $\omega_0^2 = k/I$  we obtain

$$\theta_0 e^{i\phi} = \frac{k}{N_0} \left[ 1 + i\beta(R/\delta) \left( \frac{\rho}{\rho_r} \right) \left( \frac{f}{f_0} \right)^2 - \left( \frac{f}{f_0} \right)^2 \right]^{-1}. \quad (6)$$

Here,  $f_0 = \omega_0/2\pi$  is the resonance frequency in vacuum, and the viscous dissipation function [19],

$$\beta(R/\delta) \equiv \frac{\rho_r v}{\rho I \omega}, \quad (7)$$

describes the dependence on viscosity in terms of the length ratio  $R/\delta$ . This function can be obtained from calibration with fluids of known density and viscosity. For now we use the analytical approximation of equation (2) to write

$$\beta(R/\delta) = \frac{2(1+i)}{(R/\delta) \tan[(1+i)L/\delta]}. \quad (8)$$

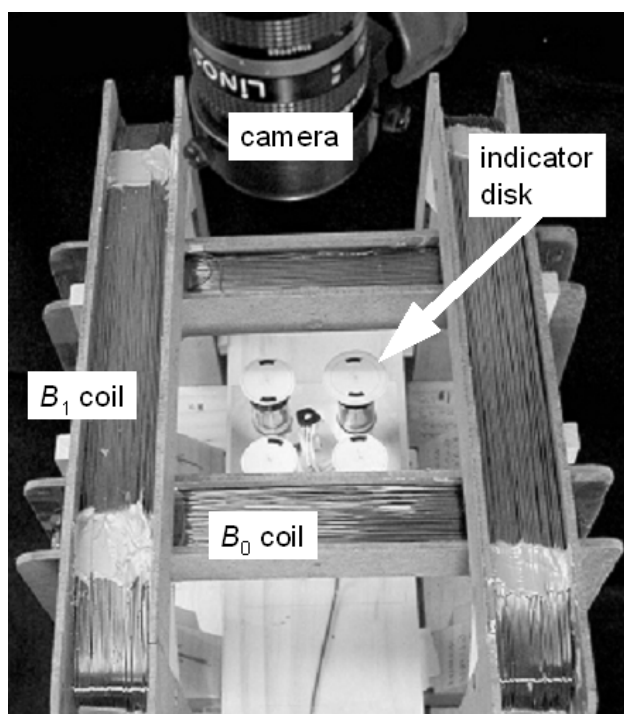


**Figure 2.** Picture of the multi-sample viscometer. The square quasi-Helmholtz coil and four test cells are shown when looking down at the instrument from an angle. The LED, used in indicating phase, is visible in the centre of the test cell array.

### 3. Apparatus construction and operation

The combinatorial viscometer is composed of three major parts. (1) The Couette sample cells. (2) A two-axis Helmholtz coil and supporting electronics to drive the magnetic fields. (3) A CCD camera and software to record and analyse the rotor responses. The prototype instrument described here<sup>4</sup> has four sample cells; however, larger arrays should be possible upon appropriate scaling of the instrument components. The test cells and Helmholtz coil construction, described in detailed below, are represented by the line drawing in figure 1 and shown in actuality in figure 2.

The Couette test cells, shown in figures 1 and 2, are composed of a glass cup and an aluminium rotor. The glass cup was made from commercially available glass vials whose inner diameter is  $(1.448 \pm 0.005)$ <sup>5</sup> cm and length (excluding the screw cap) is about 5 cm. A dimple was placed in the bottom by gently heating the inverted vial by a torch while it was centred over a sharpened rod. The centre of the bakelite screw cap was drilled with a #80 drill bit; enlarging most of the length of this hole with a larger bit minimized the contact between the screw cap and the rotor bearing wire. The screw cap was then polished under a microscope to further reduce friction with this wire.

<sup>4</sup> In order to describe materials and experimental procedures adequately, it is occasionally necessary to identify commercial products by manufacturers' names or labels. In no instance does such identification imply endorsement by the National Institute of Standards and Technology, nor does it imply that the particular product or equipment is necessarily the best available for the purpose.

<sup>5</sup> Unless otherwise specified, standard uncertainties given are based on 1 standard deviation.

The rotors were made from aluminium (alloy 2024) with a diameter of  $(0.944 \pm 0.003)$  cm and length of  $(2.04 \pm 0.01)$  cm. A small hole was drilled on a diameter at the rotor's mid height to accept a small samarium cobalt magnet, length of  $(5.5 \pm 0.2)$  mm and diameter of  $(1.12 \pm 0.03)$  mm. Stainless steel wire (diameter of 0.33 mm) was glued into axial holes in the top and bottom of the rotor with the bottom length of wire being about 1 cm and the top length being about 3.7 cm. The bottom wire was polished to a point under a microscope. The polished point on the glass dimple formed the bottom bearing of the rotor. The top wire passed through the hole in the bakelite cap to form the top bearing. Great care was taken to minimize contact areas and keep the surfaces clean in order to minimize friction. The assembled test cells each hold about 3 ml of sample and have a rotor–vial gap of  $L = (2.52 \pm 0.06)$  mm. The four assembled test cells are held in an aluminium block centred in the two-axis Helmholtz coil.

The angular displacement of the rotor in each test cell is tracked via a paper indicator disc (diameter of 2 cm) attached to the top of the rotor bearing wire. The disc was inscribed with two symmetric, opposing marks near the disc's edge (see figures 1 and 2). The displacement of these marks is recorded by the CCD camera. The two-axis (quasi) Helmholtz coil comprised 200 turns of 22 American wire gauge (AWG) copper magnet wire wound on square wooden coil forms (shown in part in figure 2). The square design was chosen to ease construction and sample placement [20, 21]. The inside coil pair (used to create the static field  $B_0$ ) has an average width of 19 cm with a separation of 10.6 cm. The outside coil pair (used to establish the ac field  $B_1(t)$ ) has an average width of 23.5 cm with a separation of 20.6 cm.

The static field  $B_0$  is typically 13.7 Gauss (G; 0.84 A) and is oriented collinear with the Earth's magnetic field. The ac field has an amplitude  $B_{10}$  that ranges from 3 to 15 G (0.24–1.12 A). This ac coil is driven by a function generator fed into a Kepco Bop-50M operational amplifier in the current-stabilized mode. Due to the reactive-load nature of the Helmholtz coil, additional capacitance ( $0.2 \mu\text{F}$ ) was added to the amplifier, following the manufacturer's instructions. Bandwidth limitations are not expected at the low frequencies, 0.05–5 Hz, typically used.

The coil currents are monitored using  $2.00 \Omega$ , 100 W sense resistors in series with each coil pair. Although the resistors have excellent temperature stability, they were thermally attached to cooling fins to ensure operation near ambient temperature. In parallel with the ac sense resistor is a circuit that drives a light emitting diode (LED) to indicate the sign, and hence the zero crossing, of the ac signal. When the signal is positive the LED is illuminated.

The CCD camera records the LED state and the positions of the indicator discs. The camera has a 1/3 inch CCD with  $512 \times 480$  square pixels, and it can record 543 full frames at 30, 60, 125, or 250 frames  $\text{s}^{-1}$ .

Custom image analysis software was developed using Interactive Data Language (IDL, Research Systems Inc.). The entire data analysis routine uses scalable arrays for data storage and manipulation to ensure ease of simultaneous calculations for multiple test cells. The software extracts the angular displacement  $\theta(t)$  of each rotor (via the indicator disc) by tracking a line connecting the centroids of the two marks on

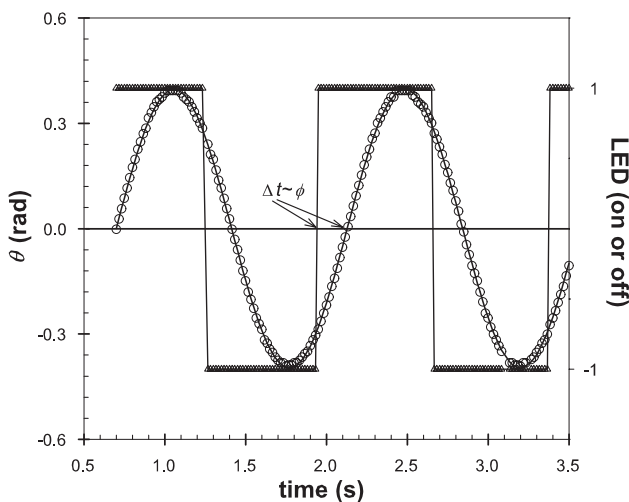


**Figure 3.** Data from the image analysis program used in finding  $\theta_0$  and  $\phi$ . The angular displacement data  $\theta(t)$  are given by the open circles while the line passing through the circles is the sinusoidal fit that determines  $\theta_0$ . The LED intensity is described as either on (+) or off (–); the data are the open triangles while the line is a guide to the eyes. The time  $\Delta t$  between the zero crossings of the two curves yields the phase  $\phi$ . Shown are data from 100 mPa s silicone oil at 0.7 Hz, with  $B_0 \approx 14$  G and  $B_{10} \approx 6.5$  G. The camera frame rate (lower than typical for data acquisition at this frequency) was 60 frames  $s^{-1}$ .

the disc. The amplitude  $\theta_0$  is determined from a least-squares fit of the data to a sine wave. The phase  $\phi$  is derived from the difference between the zero crossings of  $\theta(t)$  and  $B_1(t)$ . An average value for  $\phi$  is calculated using multiple zero crossings. Figure 3 shows representative data collected for one cell.

#### 4. Instrument characterization

The field from each coil pair was mapped by driving the pair at 1 kHz and measuring the current induced in a small test coil. Uniformity of the field was better than  $\pm 2\%$  over the volume occupied by the test cells.

The test cells are spaced on a 4 cm square grid. For small amplitudes ( $\theta_0 < 0.5$  rad), tests indicated no interaction between adjacent cells. Larger amplitudes ( $0.5 < \theta_0 < 0.7$  rad) caused only minimal interactions. We also checked for eddy current in the aluminium sample block by using a foam block instead. There was no difference for frequencies up to 5 Hz.

Each test cell requires characterization of its resonant frequency *in vacuo* and its spring constant  $k$  as a function of  $B_0$  and  $B_{10}$ . These measurements are carried out in air (as an approximation of vacuum) since measurement viscosities are typically much greater than that of air. The characterization is done one cell at a time due to the large amplitude of oscillations at resonance in air.

In the limit of 0 Hz the oscillation amplitude is simply  $\theta_0(0) = \arctan(B_{10}/B_0)$  (see appendix A). Thus, at small amplitudes and fixed  $B_0$ ,  $\theta_0(0)$  is proportional to the current  $I_{10}$  in the ac coil. Figure 4 demonstrates that proportionality by displaying  $\theta_0(0)$  for the test cells as a function of  $I_{10}$ . Furthermore, the slope  $d\theta_0(0)/dI_{10}$  was the same for all test cells made. Despite this consistency, there were differences in the resonant frequency  $f_0$  and the friction coefficient.

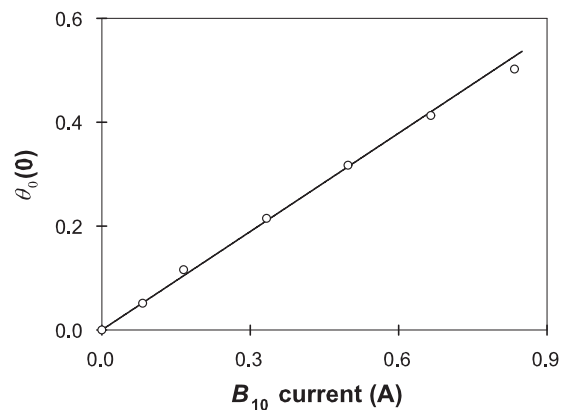


**Figure 4.** Calibration of  $\theta_0(0 \text{ Hz}) = N_0/k$  as a function of  $B_{10}$  for all of the test cells.  $B_0 \approx 14$  G.

Calibration of each test cell can account for the differences, which are likely due to geometrical variations of the rotor and its bearing wires. However, nominal values may be used without calibration when less precise, rapid screening measurements are required.

The resolution in the angular displacement  $\delta\theta$  is determined by the distance between the two marks on the indicator disc, the pixel density of the camera, and the optics plus distance between the camera and disc. For the standard setup used,  $\delta\theta = 0.0073$  rad. The resolution of the phase lag  $\delta\phi$  is determined, in part, by the camera frame rate and the frequency. If we assume the uncertainty in  $f$  is much smaller than  $\delta\phi$  we can write  $\delta\phi \sim \delta t(2\pi f)$  where  $\delta t$  is no worse than  $1/\text{frame rate}$ . For this paper, we reported the standard uncertainties either as one standard deviation or based on the resolution argument just given.

#### 5. Results and discussion

##### 5.1. A rapid screening viscometer

Operation at a low fixed frequency makes possible a ‘combi’ viscometer. Figure 5 shows a calibration curve constructed with several Newtonian fluids at 0.7 Hz. The zero-shear viscosity  $\eta_0$  is then easily estimated for multiple samples simultaneously with minimal modelling and computational effort. This approach could be used for rapid screening of fluids over two decades in  $\eta_0$ . Larger viscosities are accessible by increasing  $B_{10}$  and the gap  $L$ . Decreasing  $L$  makes smaller viscosities accessible. Although rudimentary, this approach offers simplicity and speed, which is often sufficient for screening large libraries of samples. Choice samples could then be selected for more careful measurements with this instrument or subjected to traditional rheometry.

##### 5.2. Accuracy of the model

To demonstrate the instrument we used commercially available silicone and mineral oils intended as Newtonian viscosity standards. All fluids were used without further treatment at ambient temperature ( $\approx 25$  °C). Figure 6 compares measured data with equation (6) for fluids with nominal viscosities  $\eta \approx 50, 500$  and  $2000$  mPa s. The comparison requires knowledge

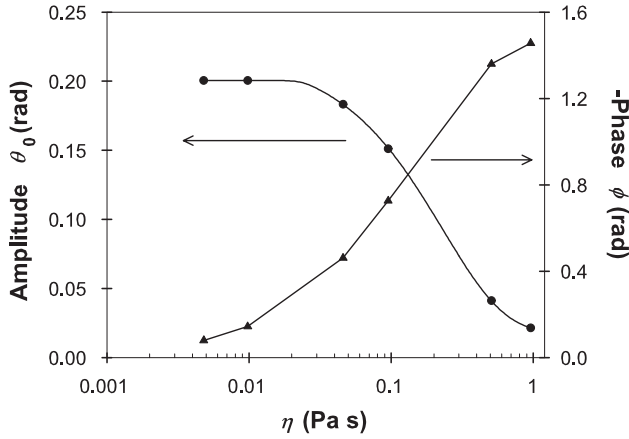


**Figure 5.** A calibration curve for rapid screening of samples at 0.7 Hz. The  $B_0$  field is about 13 G and  $B_{10} = 2.4$  G. Lines are to guide the eyes.

of the rotor's dimensions and density, the fluid's viscosity and density, and the values of  $B_0$ ,  $B_{10}$  and  $f_0$ . The model best predicts the data when the viscous term is large compared to the other two terms and to neglected effects such as secondary flows and friction. (In these cases the Reynolds number, ratio of inertial forces to viscous forces, is always less than 1.) For the 500 mPa s fluid, good agreement is observed in the amplitude  $\theta_0$ . We speculate that friction is the major contributor to deviations between the model and data. The 50 mPa s results exhibit strong deviations from the model. Here friction is important,  $Re \# \geq 1$ , and any other second-order effects have become important relative to  $\beta(R/\delta)$ .

Given that most polymer formulations are rather viscous, in its present form the model is already useful for combinatorial viscometry. We expect that accounting for bearing friction and improving the description of the viscous dissipation function  $\beta(R/\delta)$  will significantly increase the model's accuracy. These two enhancements are suggested by figure 7, which plots  $\beta(R/\delta)$ . The curve is the analytical approximation from equation (8) and the symbols were derived from measurements of  $\theta_0$  and  $\phi$  for the five Newtonian standards. The measured values used equation (6) recast as

$$\beta(R/\delta) = -\left(\frac{\rho_r}{\rho}\right) \left(\frac{f_0}{f}\right)^2 \left[ \frac{N_0}{k\theta_0} (\sin \phi + i \cos \phi) + i \left( \left(\frac{f}{f_0}\right)^2 - 1 \right) \right]. \quad (9)$$

The agreement among the fluids and between the measured and calculated values of  $\beta(R/\delta)$  is generally good. The deviations at low frequency of the low viscosity fluids are likely due to friction at the bearings. The deviations at the largest values of  $R/\delta$  are likely due to inaccuracy of equation (8).

### 5.3. Measurement of viscosity

Equating the measured value of  $\beta(R/\delta)$  from equation (9) with the calculated value of equation (8) yields the viscous penetration depth  $\delta$  and thus the viscosity  $\eta$  if the density  $\rho$  is known. For the Newtonian fluids  $\eta$  is real, so we solved for the viscosity by using only the magnitudes of equations (8)

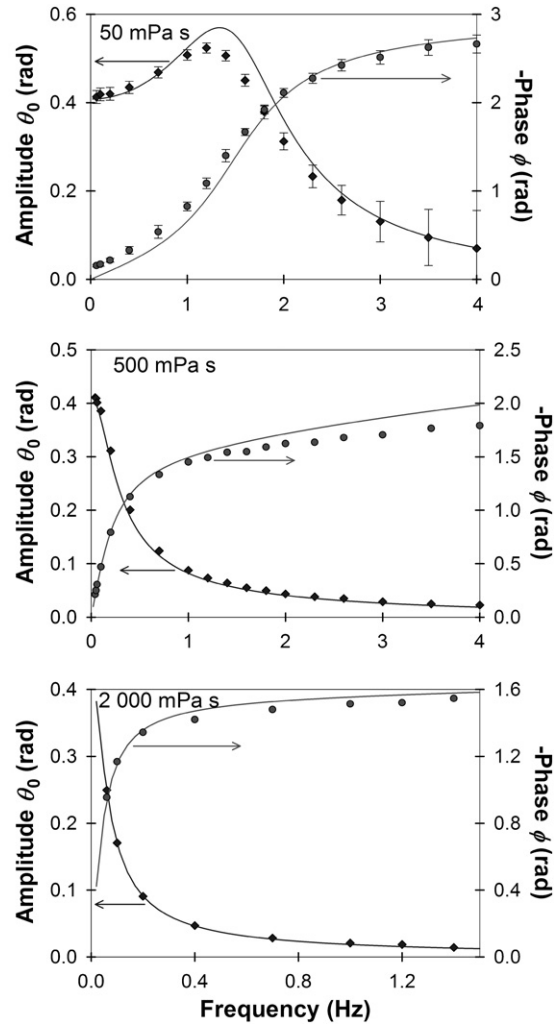
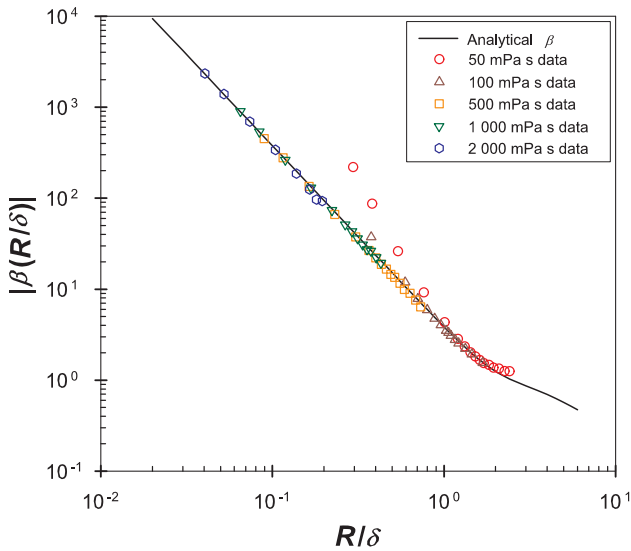


**Figure 6.** Data (symbols) and model (lines) for three Newtonian fluids. For these data sets  $B_0 \approx 14$  G,  $B_{10} \approx 6.5$  G and standard uncertainties are based on the resolution of the measurement.

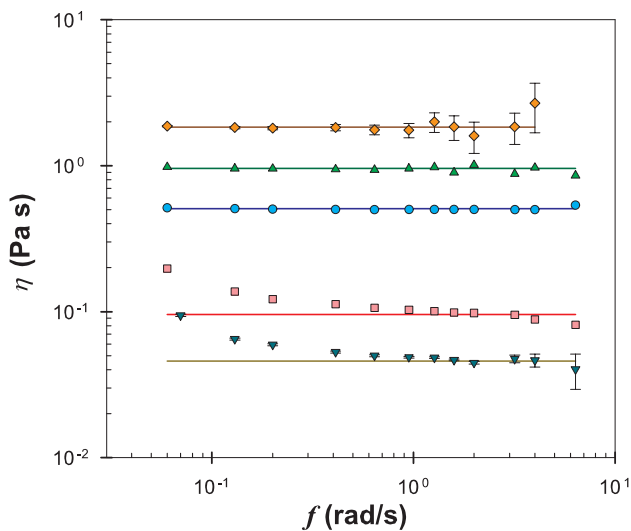
and (9). Using both the magnitude and phase of  $\beta(R/\delta)$  allows this procedure to be extended to complex viscosity. The calibration curve of figure 7 plus a corresponding curve for  $\phi$  appear sufficient to obtain the frequency dependence of linear viscoelastic fluids.

Figure 8 compares the measured viscosity at several frequencies to the viscosity expected for the Newtonian standards. Detection of the response at larger frequencies in the larger viscosity fluids was limited by camera resolution at the small  $\theta_0$ . Both the 100 and 50 mPa s fluids show strong positive deviations at low frequency, and the 50 mPa s shows an additional deviation at higher frequencies. The source of these deviations was likely due to friction and inaccuracy in  $\beta(R/\delta)$  as mentioned above. Overall, the agreement is good and we expect that refinements of the model will yield more accurate viscosity values.

The multi-sample viscometer promises a higher rate of sample throughput than a conventional rheometer. In its current inception the multi-sample viscometer requires about the same time per sample for loading and cleaning as does a typical Couette cell viscometer. At each frequency, the time to



**Figure 7.** Plots of the viscous dissipation function  $\beta$  for data (symbols) and the analytical approximation in equation (8) (curve). The large deviations at low viscosity are likely due to friction at the bearing wire. The small deviations at large  $R/\delta$  are likely due to failure of the analytical approximation.



**Figure 8.** Comparisons of the measured viscosity (symbols) with the expected value (solid lines) of five Newtonian fluids. Standard uncertainties are shown only for 2000 and 50 mPa s fluids for clarity.

collect the raw data also is comparable, but the multi-sample viscometer collects data for four samples instead of one. The image processing that converts the raw data to viscosity is currently operator intensive and requires typically 2 min per sample at each frequency. Nonetheless, processing four samples simultaneously to obtain the curves shown in figure 8 requires typically 2 h, which is comparable to the time for a single set of similar conventional rheometer measurements. Therefore, optimization of the image processing algorithm and the use of a larger sample array will give the multi-sample viscometer a clear advantage. A further advantage of the multi-sample viscometer over both conventional rheometry and particle tracking microrheology is that the samples in an array will have identical histories, an important issue in kinetic studies.

## 6. Conclusions and future work

We have designed, fabricated and demonstrated a prototype of a new multi-sample viscometer. This instrument can be used either as a rapid screening tool, employing a simple calibration curve to determine zero-shear viscosity ( $\eta_0$ ), or as an accurate viscometer, using a viscously damped oscillator model. The present device measures four samples simultaneously, and larger arrays of samples should be possible upon scaling of the instrument components.

The instrument is capable of measuring the frequency-dependent viscosity, thus suggesting the ability to measure the complex viscosity. We are further developing the model and algorithms to account for friction and to find both the real and imaginary components of the complex viscosity  $\eta^*$ . Preliminary measurements with viscoelastic fluids have already shown qualitative differences in instrument response compared to that of Newtonian fluids.

## Acknowledgments

The authors are indebted to F L Walls (Total Frequency, Boulder, CO) for design and construction of the LED circuit that indicates the current zero crossing; to Martin Misakian (NIST, Gaithersburg, MD) for his assistance in design of the square Helmholtz coils and to Chris White (NIST, Gaithersburg, MD) for stimulating discussions which eventually led to the approach we took in measuring multiple samples. We thank Kate Beers, Michael Fasolka and Kalman Migler (NIST, Gaithersburg, MD) for their encouragement and assistance in preparing this manuscript. H J Walls was a National Research Council Postdoctoral Fellow at NIST while this work was conducted.

## Appendix A. Magnetic torques on the rotor

Applying the dc magnetic field  $B_0$  causes the rotor to twist until the imbedded permanent magnet is aligned with  $B_0$ . (Scalar notation is used here because the directions of the fields and the magnetic moment  $M$  lie in the horizontal plane.) Adding the ac magnetic field  $B_1(t)$  creates the total magnetic torque,

$$N_B(t) = -MB_0 \sin[\theta(t)] + MB_1(t) \cos[\theta(t)], \quad (\text{A1})$$

where  $\theta = 0$  is defined by the direction of the dc field (see figure 1). The torque is about the rotor's vertical axis. In the limit of small oscillation angles  $\theta(t)$ , the magnetic torque is

$$N_B(t) \approx -MB_0\theta(t) + MB_1(t) \quad (\text{A2})$$

$$\equiv -k\theta(t) + N_0 \cos(\omega t), \quad (\text{A3})$$

where  $k \equiv MB_0$  is a torsion spring constant and  $N_0(t) \equiv MB_1(t)$  is the magnitude of the applied oscillatory torque. Including  $N_B(t)$  and viscous dissipation in the rotor's equation of motion yields

$$I\ddot{\theta}(t) = N_B(t) - v\dot{\theta}(t) \quad (\text{A4})$$

$$\approx -k\theta(t) + N_0 \cos(\omega t) - v\dot{\theta}(t), \quad (\text{A5})$$

which rearranges to equation (1).

Figure 4 shows that the range over which the small angle approximation is valid. The data were taken at frequencies

low enough to neglect viscosity and inertia, so the oscillation amplitude was

$$\theta_0 = \arctan\left(\frac{B_{10}}{B_0}\right) \approx \frac{B_{10}}{B_0} \left(1 + \frac{1}{3}\theta_0^2\right). \quad (\text{A6})$$

This expression indicates that oscillation amplitudes less than 0.17 rad deviate from linearity by less than 1%.

## Appendix B. Analytical approximation of the viscous dissipation coefficient

We approximated the geometry of the rotor within the cylindrical vial by that of a transversely oscillating plane separated by a distance  $L$  from a parallel stationary plane. If the oscillating plane is located at  $x = 0$  and oscillates with velocity  $v_0 e^{i\omega t}$ , the viscous force on a unit area of the plane is [18]

$$F'(t) = \frac{(1+i)\eta v_0 e^{i\omega t}}{\tan[(1+i)L/\delta]}. \quad (\text{B1})$$

Use  $F'R$  as an approximation of the viscous torque per unit area of the rotor, and integrate over the curved area of the rotor to find the total viscous torque.

$$\begin{aligned} v\dot{\theta}(t) &= (2\pi RH)F'(t)R \\ &= \frac{2\pi(1+i)R^3H\eta}{\delta \tan[(1+i)L/\delta]} \dot{\theta}(t) \end{aligned} \quad (\text{B2})$$

(The flat surface at the ends of the rotor is ignored because they are farther from the walls of the vial.)

In the limit where the gap is much smaller than the viscous penetration length ( $L \ll \delta$ ), the viscous dissipation coefficient simplifies to

$$v = \frac{2\pi R^3 H \eta}{L}. \quad (\text{B3})$$

## References

- [1] Hoogenboom R, Meier M A R and Schubert U S 2003 Combinatorial methods, automated synthesis and high-throughput screening in polymer research: past and present *Macromol. Rapid Commun.* **24** 15–32
- [2] Meredith J C 2003 A current perspective on high-throughput polymer science *J. Mater. Sci.* **38** 4427–37
- [3] Meredith J C, Karim A and Amis E J 2002 Combinatorial methods for investigations in polymer materials science *MRS Bull.* **27** 330–5
- [4] Amis E J, Xiang X-D and Zhao J-C 2002 Combinatorial materials science: what's new since Edison? *MRS Bull.* **27** 295–6
- [5] Matsieve L, Bennett J and McFarland E 2002 Method and apparatus for characterizing materials by using a mechanical resonator *US Patent* US 6,336,353 B2 Symyx Technologies, Inc., USA
- [6] McFarland E and Matsieve L 2002 Systems and methods for characterization of materials and combinatorial libraries with mechanical oscillators *US Patent* US 6,401,519 B1 Symyx Technologies, Inc., USA
- [7] Breedveld V and Pine D J 2003 Microrheology as a tool for high-throughput screening *J. Mater. Sci.* **38** 4461–70
- [8] Macosko C W 1994 *Rheology: Principles, Measurements, and Applications* (New York: VCH)
- [9] Kirschenmann L and Pechhold W 2002 Piezoelectric rotary vibrator (PRV)—a new oscillating rheometer for linear viscoelasticity *Rheol. Acta* **41** 362–8
- [10] Leyh C and Ritter R C 1984 New viscosity measurement: the oscillating magnetically suspended sphere *Rev. Sci. Instrum.* **55** 570–7
- [11] James S L and Marriott C 1982 A modified oscillating sphere magnetic microrheometer for use with biological secretions *J. Phys. E: Sci. Instrum.* **15** 179–80
- [12] Keller M, Schilling J and Sackmann E 2001 Oscillatory magnetic bead rheometer for complex fluid microrheometry *Rev. Sci. Instrum.* **72** 3626–34
- [13] Royer J R *et al* 2002 Polymer melt rheology with high-pressure CO<sub>2</sub> using a novel magnetically levitated sphere rheometer *Polymer* **43** 2375–83
- [14] Chu B 1989 Magnetic needle rheometer *Rev. Sci. Instrum.* **60** 3047–50
- [15] Ding J, Warriner H E and Zasadzinski J A 2002 Magnetic needle viscometer for Langmuir monolayers *Langmuir* **18** 2800–6
- [16] Bano M, Straharsky I and Hrmo I 2003 A viscosity and density meter with a magnetically suspended rotor *Rev. Sci. Instrum.* **74** 4788–93
- [17] Borghesani A F and Santini M 1989 Magnetic rotating disc viscometer *Int. J. Thermophys.* **10** 917–27
- [18] Landau L D and Lifshitz E M 1959 *Fluid Mechanics* (London/Reading, MA: Pergamon/Addison-Wesley)
- [19] Berg R F 1995 Hydrodynamic similarity in an oscillating-body viscometer *Int. J. Thermophys.* **16** 1257–66
- [20] Firester A H 1966 Design of square Helmholtz coil systems *Rev. Sci. Instrum.* **37** 1264–5
- [21] Misakian M 2000 Equations for the magnetic field produced by one or more rectangular loops of wire in the same plane *J. Res. NIST* **105** 557–64